https://doi.org/10.20965/jdr.2021.p0658

Paper:

Rigorous Analysis of Stress-Dependent Landslide Movements with Groundwater Fluctuations Applicable to Disaster Prevention in Monsoon Asia

Deepak Raj Bhat[*1,†], Soichiro Osawa[*2], Akihiko Wakai[*2], Katsuo Sasahara[*3], Netra P. Bhandary[*4], Fei Cai[*2], Hirotaka Ochiai[*5], and Norihiro Tanaka[*1]

[*1]Okuyama Boring Co., Ltd.
3-5-9 Higashi-nihonbashi, Chuo-ku, Tokyo 103-0004, Japan
[†]Corresponding author, E-mail: deepakbhat@okuyama.co.jp
[*2]Gunma University, Gunma, Japan
[*3]Kochi University, Kochi, Japan
[*4]Ehime University, Ehime, Japan
[*5]Japan Forest Technology Association, Tokyo, Japan
[Received December 7, 2020; accepted February 10, 2021]

In this study, novel finite element approaches are proposed for numerical analysis of stress-dependent landslide movement with groundwater fluctuation by rainfall. Two new constitutive parameters that are capable of directly controlling the relationship between the apparent factor of safety and sliding velocity are incorporated into a specific material formulation used in finite element analysis for the first time. For the numerical simulation of the measured time history of the sliding displacement caused by the groundwater fluctuations, such required analytical parameters can also approximately be determined by back analysis. The proposed models are applied to a landslide field experiment on a natural slope caused by rainfall in real time in Futtsu City, Chiba Prefecture of Japan to check its applicability. The predicted and measured time histories along the horizontal direction on the upper, middle, and lower slope are compared. In addition, the deformation pattern, shear strain pattern, and possible failure mechanisms of the natural slope of such a field experiment landslide are discussed in detail based on the analysis results of the finite element method (FEM)-based numerical simulation. Moreover, the creeping landslides and possible landslide sites for further application of the proposed models are briefly discussed in the cases of Nepal and Japan as examples in Asia. It is believed that the proposed newly developed numerical models will help in understanding the secondary creep behavior of landslides triggered by extreme rainfall, and at the same time, long-term management of such landslides will be much easier in monsoon Asia. Finally, it is expected that this study will be extended for simulation of the tertiary creep behavior of landslides induced by rainfall in the near future.

Keywords: monsoon, sliding velocity, factor of safety, finite element method, constitutive model of soil

1. Introduction

1.1. Background

Soil creep is a time-dependent phenomenon in which a deformation emerges under the application of constant stress. Theoretically, the different stages of creep are defined based on the ideal creep curve concept, in which different stages of creep depend upon the strain rate. In the first stage of creep, the strain rate decreases continuously with time; this is called the primary stage of creep. After this, a constant strain rate emerges, which is called the secondary stage of creep. Finally, the strain rate suddenly increases, which leads to a failure of the soil, which is called the tertiary stage of creep. Terzaghi [1] was most likely the first to consider the relationship between soil creep and landslides. Ter-Stepanian [2] introduced the threshold approach to explain soil creep in simple natural slopes by considering the zone of creep and its rate as being dependent on the groundwater level. Eyring [3] introduced the theory of rate processes based on the idea that the strain process consists of the mutual displacement of flow units by surmounting energy barriers and is quite promising in prospect. Shimokawa [4] discusses the creep deformation and creep strength of cohesive soils and their relationship to landslide based on experimental and theoretical studies using the rate process theory. Feda [5] has also interpreted the creeping behavior of soils using the rate process theory.

Murayama and Shibata [6] and Christensen and Wu [7] have developed rheological models to represent the time-dependent behavior of soil. Ter-Stepanian [8] proposed a rheological model to understand the creeping behavior of clayey soils during shear. In several publications about the rheological creep behavior of soils to evaluate the range of creep, Ter-Stepanian [8] explains that soil viscosity is pos-

itively related to a soil structure deformability coefficient. Further investigation on Ter-Stepanian's [2] creep model has been done by Yen [9], and an apparent creep threshold line (yield strength line) is described, where the material is in a creep phase. In addition, Yen [9] concludes that creep deformation is ensured when the shear stress due to gravity exceeds the soil residual shear strength, and Suhaydu and Prior [10] and Iverson [11] also agree upon this.

Sekiguchi and Ohta [12] and Zhou et al. [13] proposed the time-dependent anisotropic model, which assumes fixed anisotropic models. Desai et al. [14] proposed a constitutive model for describing the creeping behavior of natural slopes. In parallel, Pestana and Whittle [15], Wheeler et al. [16], and Dafalias et al. [17] proposed time-independent anisotropic models accounting for both initial and evolving anisotropy. A new anisotropic viscous model based on Wheeler et al.'s [16] model has been proposed by Leoni et al. [18] to understand the rate-dependent behavior of soft soils. Liingaard et al. [19] presented a comparative study on creep models. Calvello et al. [20] presented an extensive study using a numerical model that focuses on active landslides controlled by rainfall-induced pore pressure fluctuations with movements concentrated within a relatively narrow shear zone above which the sliding mass moves essentially as a rigid body. Leoni et al. [18] presented a new anisotropic model for the time-dependent behavior of soft soils using triaxial compression test data. Huvaj and Maghsoudloo [21] used a simple Mohr-Coulomb constitutive model to model a slow-moving landslide in Italy using the computer program PLAXIS. Fernández-Merodo et al. [22] proposed a two-dimensional viscoplastic finite element model for slow-moving landslides and also applied this model to the Portalet landslide of Spain as a case study. A new concept of the residual-state creep test and a new testing setup and method for residual-state creep have been developed by Bhat et al. [23, 24]. Based on that apparatus and method, the residual-state creep behavior of artificial clay and landslide clay has been studied [25, 26]. Bhat and Yatabe [27] proposed a new regression model to understand the creeping behavior of clayey soils at the residual-state of shear.

Creeping landslides are controlled by groundwater fluctuations [2, 14, 28–31]. Therefore, groundwater fluctuations should be incorporated into the numerical simulation of such landslides. However, most of the previous numerical approaches [2, 5, 9, 18, 31–36] to soil creep and associated problems have focused on laboratory creep tests (i.e., consolidation/oedometer test and triaxial test), which could not address the fluctuation of groundwater level. Huvaj and Maghsoudloo [21] simulated the fluctuation of groundwater level in different phases to understand the creeping behavior of a slow-moving landslide, but the exact value of the deformation at any required point (location) could not be captured perfectly. Recently, a few researchers [22, 28, 29, 37] have proposed a two-dimensional Elasto-viscoplastic constitutive model using the finite element method based on the field instrumentation and monitoring results, but they only considered a single control constitutive parameter based on the trial and error method, which could not control the displacement rate of the landslide and also far from addressing the realistic field problem of the creeping behavior of landslides. Therefore, if a new numerical approach, which can incorporate more than one control constitutive parameter for directly controlling the displacement rate and total factor of safety of the landslide, can be developed, such approach may be useful for investigating the realistic field problem of the creeping displacement behavior of landslides in the future.

The main objective of this study is to address the above-mentioned problems to understand the creeping behavior of landslides using a newly developed finite element-based numerical model and its implications for disaster prevention in monsoon Asia. The specific objectives include the following: i) to present the current creeping landslide scenario in Nepal and Japan as examples of Asia while searching for the possibility of application of the proposed numerical models in the cases of Nepal and Japan in the near future; ii) to propose a simplified procedure for the determination of two new control constitutive parameters; iii) to estimate such new control constitutive parameters based on the relation between the apparent factor of safety and sliding velocity using the finite element method (FEM); iv) to propose a new numerical approach to evaluate the creeping behavior of landslides owing to groundwater fluctuations due to rain water; v) to understand the failure mechanisms along the slip surface of creeping landslides triggered by extreme rainfall; vi) to apply the proposed models to understand the creeping behavior of a landslide field experiment on a natural slope in Futtsu City of Chiba Prefecture, Japan, for the validation of the newly developed numerical models; and vii) to present the simulation results of the deformation pattern and shear strain pattern and discuss the possible failure mechanisms of the slope based on variations in the local factor of safety and mobilized shear strength along the slip surface.

1.2. Creeping Landslides in Nepal and Japan: Examples in Asia

Landslides are one of the major natural disasters in Asia during the monsoon period. They have claimed thousands of human lives and extended economic losses of billions of dollars in individual property and infrastructure damage each year, especially during the monsoon period. The disaster records of Asian countries show that the frequency of fatal landslides was highest in China, followed by Indonesia, India, the Philippines, Japan, Pakistan, and Nepal between 1950–2009 [38]. Therefore, a heavy amount of the national budget of Asian countries has been spent on the prevention and mitigation of these landslides, in which the major interest remains minimizing the creeping displacement of these landslides, thereby reducing the damage risk to human settlements and structures over the landslide mass or to the environment. However, the creep

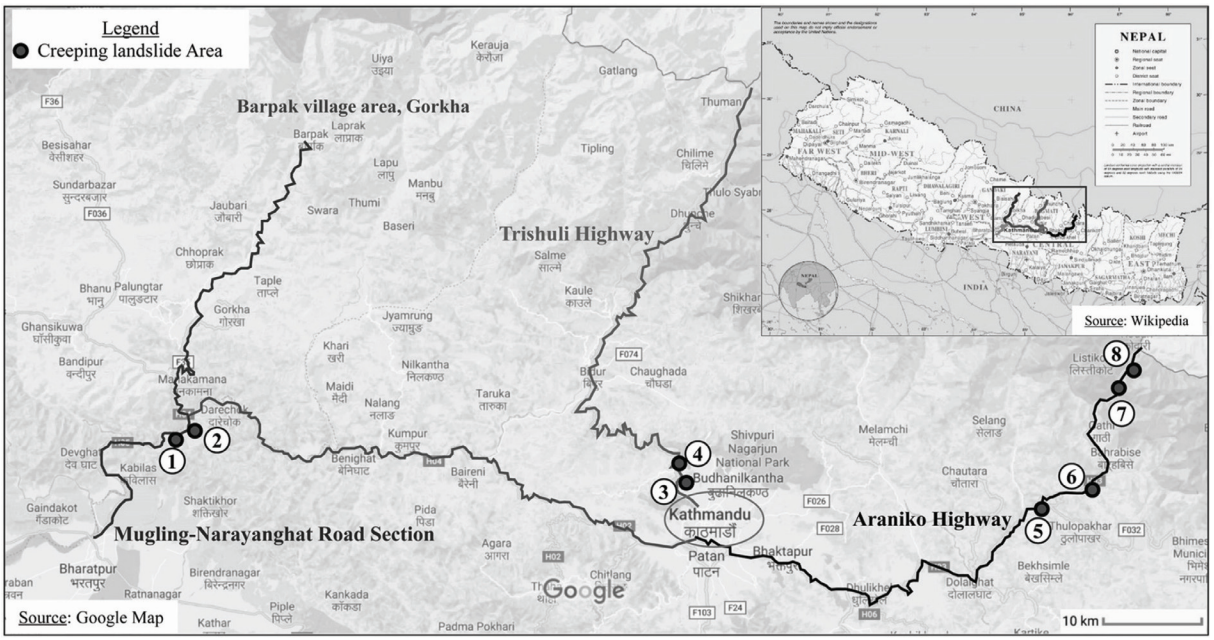

Fig. 1. Location of selected creeping landslides for further application of the proposed model in Nepal.

behaviors of such landslides and the associated geological and geotechnical issues are not fully understood, so it is difficult to predict the creep displacement behavior of landslides, which may be useful for the design of countermeasure works for these landslides in the future. On the other hand, although the creep displacement behavior of landslides is very important, such creep displacement behavior and its associated problems of landslides have not been considered during the stability analysis of slopes and landslide countermeasure works until now. In this paper, creeping landslides in Nepal and Japan are briefly discussed as examples in Asian countries.

Nepal is a highly mountainous country that is covered by mountainous and hilly regions in more than 80% of the area. Nepal has been formed by the collision of the Indian and Eurasian plates, which occupy approximately 800 km along the central part of the Himalayan arc. A huge variation of topography from less than 60 m in the Southern Terai plain to 8848 m at Mount Everest in the norther Higher Himalayas within an average lateral distance of less than 200 km characterizes the steep topography of Nepal [39, 40]. This kind of topography is prone to landslides in Nepal [40]. Large-scale landslides are very common in the Lesser and Higher zones of the Nepal Himalayas due to the steep mountainous slopes and dynamic geological conditions [40]. Based on a database study of landslides from 1978–2005, Petley et al. [41] state that here is a high level of variability in the occurrence of landslides from year to year in Nepal.

In Nepal, monsoons are a major source of rainfall in summer, and approximately 80% of the total annual precipitation takes place during the monsoon period (i.e., June to September) [39]. The annual average rainfall is about the 1600 mm and approximately 2000–3000 mm in the central part of Nepal. During the rainy season, daily distribution of the precipitation is also uneven. For example, sometimes 10% of the total annual precipitation occurs per day and 50% of the total annual precipitation per 10 days occurs during the monsoon period [39]. Therefore, such type of uneven distribution of precipitation may play an important role in triggering creeping landslides in Nepal. According to Petley et al. [41], there is a strong increasing trend in the number of fatalities occurring in Nepal at any point in the monsoon cycle.

In this context, the first and third authors visited the different landslide areas along the major highway and Barkpark area of Gorkha in August 2017 for detailed observation and sampling of the creeping landslide sites of Nepal. During this visit, they observed a few old activated creeping landslides and also identified a few newly activated creeping landslides [42]. **Fig. 1** shows the location of the few representative creeping landslides, such as the Narayanghat-Mugling creeping landslide (Block I) and the Narayanghat-Mugling creeping landslide (Block II) along the Narayanghat-Mugling road section, the Jalkini creeping landslide and Okharpuwa creeping landslide along Trishuli highway, as well as the Balefi creeping landslide, Jure creeping landslide, Hindi creeping landslide, and Tusare-Batish creeping landslide along the Araniko highway, which seems applicable for the further study using this newly developed FEM-based numerical model in the near future. The soil samples from these landslide sites were collected, and further laboratory investigations have also been performed. Such field and lab investigation results will be useful in estimating the landslide simulation parameters for the application of the proposed numerical model for numerical analysis of those landslides in the near future. **Figs. 2–4** show representative creeping landslides in Nepal. The scenario of creeping landslides in Nepal has been discussed based on

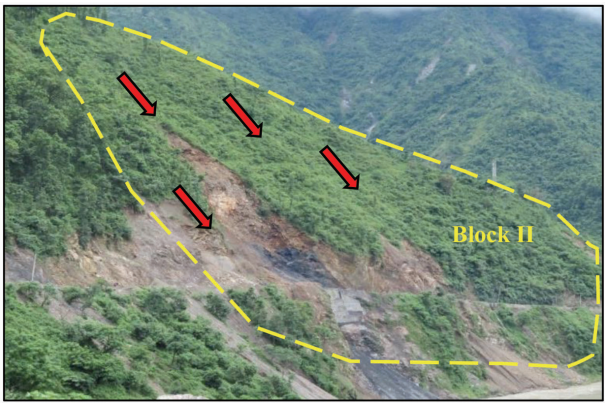

Fig. 2. View of Narayanghat-Mugling creeping landslide (Block II), Chitwan, Nepal.

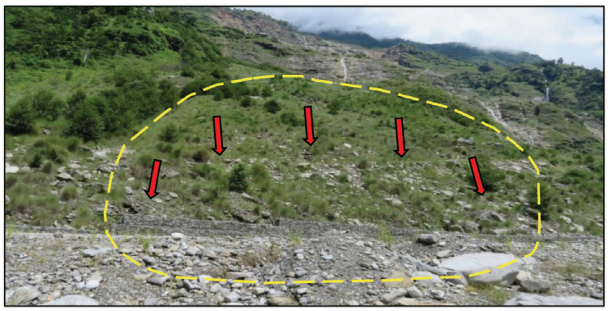

Fig. 3. View of Jure creeping landslide, Sindupalchok, Nepal.

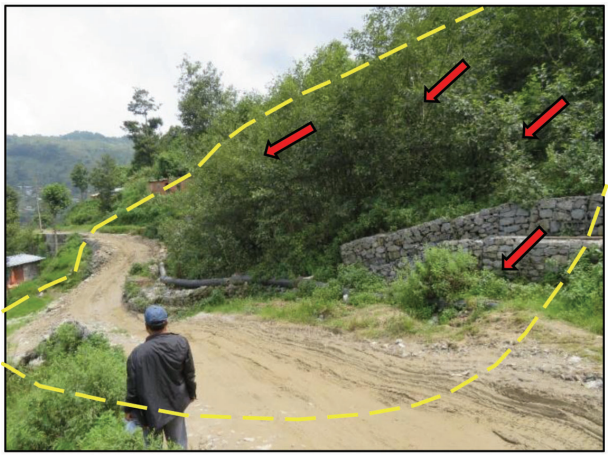

Fig. 4. View of Okharpuwa creeping landslide, Nuwakot, Nepal.

field observation and laboratory investigation of eight representative creeping landslides of Nepal [42].

During the field observation in Nepal, it was observed that a large number of human settlements and rapid infrastructure developments are situated either on old or newly activated creeping landslide masses or on or near creeping landslide-prone areas, especially in the mountainous regions of Nepal. Landslides are a major problem in Nepal, causing high levels of economic loss and substantial numbers of fatalities each year [41]. There is a similar situation in many other Asian counties. Therefore, the damage to lives, properties, infrastructure, and the environment are gradually increasing day by day due to rainfall-induced landslides and the associated creeping phenomenon in Asian countries during monsoon season.

Similarly, Japan is also a mountainous country, where 75% of the total land area consists of mountainous terrain, and the remaining 25% is flat and low lying with plateaus. Therefore, Japan has suffered from numerous landslide disasters since ancient times. On the other hand, many people have lived in the mountainous region since ancient times. Therefore, damage caused by landslide disasters, especially creeping landslides, has been playing a major role in influencing the quality of life [43]. Wakai et al. [44] and Bhat et al. [45] reported that many creeping landslide sites accommodate human settlements, agricultural fields, roads and highways, bridges and tunnels, and nature conservation sites in Japan. When the displacement rate of such landslides is suddenly increased and accelerated, it leads to significant mass failure, which damages human lives, property, nature, and the environment. If some approaches to predicting the creep failure of landslides are possible, all damage from such landslide disasters can be prevented [25, 46]. Therefore, a study of the creeping behavior of landslides and the associated geological and geotechnical engineering issues toward creep failure prediction seems very important in Japan.

The geology of Japan is fragile due to the plate-tectonic activities of the four major plates (i.e., North American plate, Pacific plate, Eurasian plate, and Philippine plate) along the Japanese archipelago in the north-south direction, which is the one of the major causes of the activation and reactivation of creeping landslides in Japan [43, 45]. Creeping landslides are one of the major natural disasters in mountainous regions of Japan and are mainly triggered by tectonic activities, occasional volcanic activities, heavy rainfall events, or a combination of themes [44, 47, 48]. Continuous high-intensity rainfall has been found to play a key role in provoking landslide movement [49]. Sasaki et al. [50] revealed that soil creeps usually occur during and after rain on the north side of the Tsukuba Mountain in Japan. Ogita et al. [51] discuss the shapes and mechanisms of large-scale creeping landslides in Japan. Bhat et al. [45] investigated the preexisting shear surfaces of reactivated landslides in Nepal and Japan and highlight the importance of the study of creep displacement behaviors of landslides in Nepal and Japan. Wakai et al. [44] discuss the finite element-based numerical simulation of creeping landslides in Japan and its implication for long-term monitoring and management of such landslides in the future.

The Japan Landslide Society [43] has introduced 27 representative landslides and slope failures all over Japan. The Japan Landslide Society [43] has also highlighted that several landslide mitigation measures are conducted in these landslide areas in order to stop or reduce the landslide movement so that the resulting damage can be minimized. However, the movement of such land-

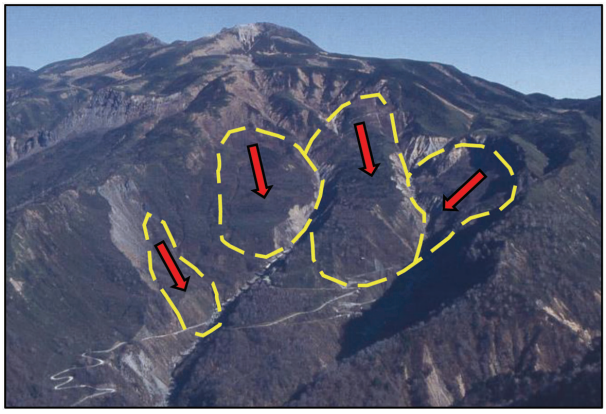

Fig. 5. View of Jinnosuke-dani creeping landslide, Haku-san Mountain area, Japan [52].

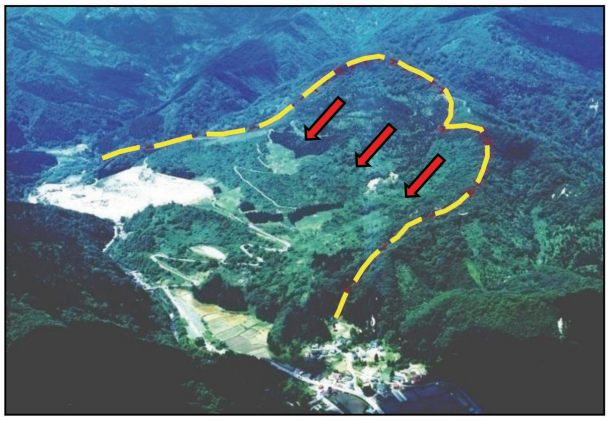

Fig. 6. View of Tozawa creeping landslide, Akita, Japan (Source: Yuri Forestry Office, Akita Prefectural Government, Japan).

slides is not totally controlled or stopped even now. It is also well understood that most of such landslides are reactivated due to the fluctuation of groundwater level, mainly in rainy seasons. Therefore, it is believed that the proposed models in this study would be useful for better understanding stress-dependent landslide movement with groundwater fluctuations for such representative landslides and slope failure, and at the same time, mitigation measures for long-term management of such landslides will be made easier in the near future. **Figs. 5–7** show a few representatives creeping landslides in Japan, where the Okuyama Boring Co., Ltd. (the first and last authors) is currently working. Recently, the authors (first, second, and last) have also been searching for the possibility of application of the proposed numerical models in these representative landslide sites as case studies in Japan.

For most Asian countries, regular monitoring (i.e., measuring the movement rate with groundwater fluctuations with respect to time) results of creeping landslides is still lacking. On the other hand, most creeping landslides are in mountainous regions and remote areas, where regular field monitoring of such landslides is also difficult and time consuming [44, 45]. Hence, it

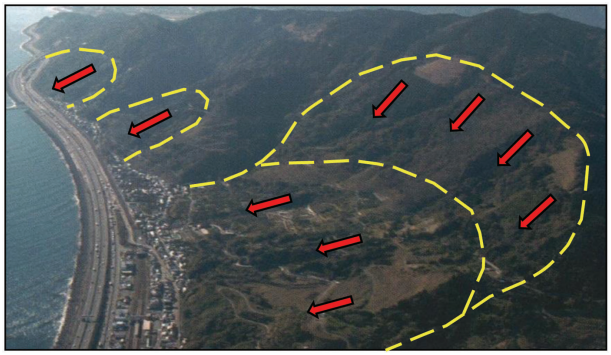

Fig. 7. View of Yui creeping landslide, Shizuoka, Japan [53].

seems almost impossible to complete landslide displacement predictions based on field monitoring results and, at the same time, long-term management of such landslide sites in the near future. Therefore, if a numerical tool or model that will be capable of better understanding the creep displacement behavior of landslides induced by rainfall and also predicting landslide displacement is needed. Then, the significant damage to lives, properties, and the environment from such landslide problems can be mitigated. Therefore, we apply our newly developed numerical models to a few landslide sites as case studies of Nepal and Japan for landslide displacement prediction in the near future (**Figs. 2–7**). Later, we will apply such models in cases of other Asian countries.

2. Proposed Finite Element Analysis Method

2.1. Factor of Safety and Sliding Velocity

Based on an extensive literature survey, Vulliet and Hutter [54] proposed an empirical relation between sliding velocity and stress state. Following the Vulliet and Hutter [54], Sugawara [55] proposed a relation between the overall factor safety (F_s) and the sliding velocity (v) of a slope on a power function, as shown in Eq. (1).

$$F_s = \left(\frac{v}{A}\right)^{\frac{-1}{n}}, \quad \ldots\ldots\ldots\ldots\ldots\ldots \quad (1)$$

where, A (velocity dimension) and n (dimensionless) are constants.

For the application of such a concept to the two-dimensional finite element method, the sliding velocity (v) assumes a translational motion and is replaced by the maximum displacement or strain rate ($\dot{\gamma}_{\max}$) of each element. Additionally, for the elasto-plastic finite element method, the overall factor safety (F_s) of a slope has been replaced by the local factor of safety ($F_{s,local}$) to reach the plastic state of each element. After redefining each constant to balance dimensions on both sides of the equation, the following Eq. (2) is obtained.

$$\dot{\gamma}_{\max} = \frac{\dot{\alpha}}{F_{s,local}^{n}}, \quad \ldots\ldots\ldots\ldots\ldots\ldots \quad (2)$$

where, $\dot{\alpha}$ (dimension of time^{-1}) and n (dimensionless) are constants.

c' and φ' are the cohesion force and internal friction angle of soil, respectively. $x-y$ represents the direct component along the x and y direction of the Cartesian coordinate system.

$$\gamma_{\max} = \sqrt{(\varepsilon_x - \varepsilon_y)^2 + {\gamma_{xy}}^2}, \quad \ldots\ldots\ldots \quad (3)$$

$$F_{s,local} = \frac{\dfrac{\sigma'_x + \sigma'_y}{2}\sin\varphi' + c'\cos\varphi'}{\sqrt{\left(\dfrac{\sigma'_x - \sigma'_y}{2}\right)^2 + {\tau_{xy}}^2}}. \quad \ldots\ldots \quad (4)$$

The details will be described later in Section 2.3. The magnitude of the maximum displacement rate under an arbitrary stress condition is defined based on Eq. (2). Similarly, the maximum displacement ($\gamma_{\max}$) at each node and local factor of safety ($F_{s,local}$) at each element are defined by following Eqs. (3) and (4), respectively.

On the other hand, Sugawara [55] proposed the empirical relation (a linear function) by direct plotting of both factors of safety and landslide displacement rate in a semi-log graph. Following this concept of Sugawara [55], we also propose Eq. (5), as shown below.

$$\dot{\gamma}_{\max} = \dot{\beta} \times 10^{m(1-F_{s,local})}, \quad \ldots\ldots\ldots \quad (5)$$

where, $\dot{\beta}$ (dimension of time^{-1}) and m (dimensionless) are constants.

A series of tests have been performed to check the applicability of both proposed models based on Eqs. (2) and (5) in real field problems by Bhat et al. [47, 56]. They have concluded that there are slight changes in the analysis results obtained from both proposed methods. Therefore, the other proposed model based on Eq. (5) is not considered in this study.

2.2. Outline of Nonlinear Analysis

In this study, the authors have simplified the elasto-plastic finite element analysis code GA3D [57] into a two-dimensional plane strain condition and a calculation algorithm that can reproduce the time-dependent behavior.

First, in order to generate an initial stress field under the stable conditions with low groundwater level, the self-weight of the entire system is used as the acting external force vector ($\boldsymbol{f_0}$) by balance calculating the overall stiffness matrix ($[K]$) of the system and the initial displacement vector ($\boldsymbol{u_0}$), as shown below in Eq. (6).

$$[K]\boldsymbol{u_0} = \boldsymbol{f_0}. \quad \ldots\ldots\ldots\ldots\ldots \quad (6)$$

Let $\boldsymbol{u_0}$ be the initial value of the displacement vector ($\boldsymbol{u}$) at each node. $\boldsymbol{u_0}$ has no physical meaning because it is an intrinsic displacement that occurs when the slope is formed. To obtain the stress increment vector ($\Delta\boldsymbol{\sigma}'$) for each element, Eq. (7) is used based on the element displacement increment vector ($\Delta\boldsymbol{u}_{elem}$), where $\Delta\boldsymbol{u}_{elem}$ is obtained by only extracting the nodal components of each element from the overall node displacement vector ($\boldsymbol{u_0}$).

$$\Delta\boldsymbol{\sigma}' = [D][B]\Delta\boldsymbol{u}_{elem}. \quad \ldots\ldots\ldots\ldots \quad (7)$$

$[B]$ and $[D]$ are the B and D matrices of each element. In the elastic-state, $[D]$ is obtained from Young's modulus of elasticity (E) and Poisson's ratio (ν) based on Hooke's law (i.e., elastic modulus matrix $[D^e]$), but in the plastic-state, the elastoplastic coefficient matrix $[D^{ep}]$ is used, as shown in Eq. (8).

$$[D^{ep}] = [D^e] - \frac{[D^e]\left(\dfrac{\partial g}{\partial \boldsymbol{\sigma}'}\right)\left(\dfrac{\partial f}{\partial \boldsymbol{\sigma}'}\right)^T[D^e]}{-\dfrac{\partial f}{\partial h}\left(\dfrac{\partial h}{\partial \boldsymbol{\varepsilon_p}}\right)^T\left(\dfrac{\partial g}{\partial \boldsymbol{\sigma}'}\right) + \left(\dfrac{\partial f}{\partial \boldsymbol{\sigma}'}\right)^T[D^e]\dfrac{\partial g}{\partial \boldsymbol{\sigma}'}}, \quad \ldots\ldots\ldots\ldots\ldots\ldots \quad (8)$$

where f is the yield function, and g is the plastic potential. In this analysis method, strain softening is not considered; hence, the hardening parameter is assumed to be zero (i.e., $h = 0$). Both the yield function (f) and the plastic potential (g) are defined based on the Mohr-Coulomb type equations, as shown in Eqs. (9) and (10).

$$f = \sigma'_1 - \sigma'_3 - 2c'\cos\varphi' - (\sigma'_1 + \sigma'_3)\sin\varphi', \quad \ldots \quad (9)$$

$$g = \sigma'_1 - \sigma'_3 - (\sigma'_1 + \sigma'_3)\sin\psi, \quad \ldots\ldots \quad (10)$$

where σ'_1 and σ'_3 are the maximum and minimum principal stresses, and ψ is the dilatancy angle. Under non-drained (i.e., equal volume) conditions, $\psi = 0$.

Each stress component will be updated by cumulatively adding the stress increment vector ($\Delta\boldsymbol{\sigma}'$) from Eq. (7) to the stress vector ($\boldsymbol{\sigma}'$) (initially zero) of each element. At this time, a correction is needed to fix and pull back the constant J_2 up to the yield surface to prevent the drifting of stress points from outside of the yield plane [58].

The equivalent nodal force vector ($\boldsymbol{f}$) is back calculated (the sum of the total stress component vector ($\boldsymbol{\sigma}$), which is obtained by adding the pore water pressure to the normal stress component of the effective stress ($\boldsymbol{\sigma}'$) of each element) from the stress distribution obtained as above.

$$\boldsymbol{f} = \int_V [B]^T\boldsymbol{\sigma}\,dV. \quad \ldots\ldots\ldots\ldots \quad (11)$$

If all elements are in the elastic state, then, $\boldsymbol{f} = \boldsymbol{f_0}$. Therefore, an iterative calculation due to material nonlinearity is not necessary. However, the plastic-state is normally occurring in some elements.

In general, the external loading force ($\boldsymbol{f_0}$), which acts in the first stage of forming the initial stress field, is extremely large. Therefore, it will not converge if the generated stress increments are collectively subjected to the elasto-plastic processing using Eqs. (7) and (8). Hence, the shear strength reduction method (SSRM) [59] is used for the convergence of it in the given initial condition. In this method, a large shear strength is assumed in the elastic-state at first, and then, it is gradually decreased and reaches the plastic region. Finally, the imbalance force is balanced by the number of iterative calculations.

The process of nonlinear iterative calculation within one calculation step of the shear strength reduction method is described below. When any element reaches the plastic-state, the residual force vector, $\Delta \boldsymbol{r}$ $(= \boldsymbol{f_0} - \boldsymbol{f})$ is obtained, and it is distributed to the entire system by the modified Newton-Raphson method.

$$[K]\Delta \boldsymbol{u} = \Delta \boldsymbol{r}. \quad \ldots \quad (12)$$

As in Eq. (12) above, the initial stiffness matrix ($[K]$) is used to obtain the residual displacement increment vector ($\Delta \boldsymbol{u}$) for the external force ($\Delta \boldsymbol{r}$). It is update by adding $\Delta \boldsymbol{u}$ instead of $\boldsymbol{u}$. In addition, $\Delta \boldsymbol{\sigma}'$ is obtained from Eq. (7) using the element displacement increment vector ($\Delta \boldsymbol{u}_{elem}$), which is obtained by only extracting the nodal components of each element from $\Delta \boldsymbol{u}$. Moreover, a new residual force ($\Delta \boldsymbol{r}$) is obtained based on Eq. (11), and the next $\Delta \boldsymbol{u}$ is obtained from Eq. (12) in the next.

While repeating such calculations and updating $\boldsymbol{\sigma}$ and $\boldsymbol{u}$, the norm of the residual force ($\Delta \boldsymbol{r}$) becomes sufficiently small, and the iterative calculations will converge. After the convergence, the procedure proceeds to the next step in the shear strength reduction method (slightly reducing the shear strength), and the convergence calculation may be repeated.

After the initial stress distribution is obtained, it will move to the time history analysis considering the groundwater level fluctuations for each time step. It is noted that the groundwater level has greatly varied at different locations of the slope. Here, the hydrostatic pressure is only considered, and the fluctuation of the pressure head due to permeability is ignored. Each effective stress component of each element is obtained based on the pore water pressure, which is obtained from the corresponding groundwater depth; hence, the plasticity analysis is performed using Eq. (9). Similarly, in the case of elastic-state, $[D] = [D^e]$, and $[D] = [D^{ep}]$ for the case of the plastic-state, and the stress increment vector ($\Delta \boldsymbol{\sigma}'$) is calculated from Eq. (7). After that, the balance of the entire system from the modified Newton-Raphson method using Eqs. (11) and (12) is obtained the same as the initial stress analysis. After the calculation is converged, it will move to the calculation for the next time step (i.e., input a new groundwater level). By repeating this process, the sequential time history analysis is performed by inputting the groundwater level fluctuations up to the predetermined time.

2.3. Constitutive Law Considering the New Viscosity Formulation

In the nonlinear calculation algorithm described in Section 2.2, the constitutive law of soil is necessary for considering Eq. (2). The interested material is a group of thin slip/sliding elements that are formed along the sliding surface of the slope, and all these elements are simply sheared uniformly (i.e., the local safety factor ($F_{s,local}$) of all elements is equivalent or equal. Let us assume that the local safety factor ($F_{s,local}$) of such elements is equal to the overall safety factor (F_s) (i.e., $F_{s,local} = F_s$).

$$\dot{\gamma}_{\max} = \frac{\dot{\alpha}}{F_s^n}. \quad \ldots \quad (13)$$

However, the acting stress and strain rate ($\dot{\gamma}_{\max}$) along the slip surface are not uniform in the actual case and often exhibit a progressive failure pattern. In other words, the magnitudes of shear stress and shear strain assigned to each element are different, but the sum of the shear resistance of all elements along the sliding surface is always in balance with the driving force of the sliding mass. Since the magnitude of the strain rate generated in each element is obtained as a result of such a balance calculation of the whole system, the strain rate is at least controlled by the local safety factor ($F_{s,local}$) of all elements. Hence, the strain rate ($\dot{\gamma}_{\max}$) should be less than or equal to the right side of Eq. (2). Therefore,

$$\dot{\gamma}_{\max} \leqq \frac{\dot{\alpha}}{F_{s,local}^n}. \quad \ldots \quad (14)$$

On the other hand, let us consider a case where the local factor of safety ($F_{s,local}$) of all elements is equal for satisfying Eq. (14); then, the strain rate ($\dot{\gamma}_{\max}$) of all elements is equal, and it is obvious that it should not contradict Eq. (13). Based on the consideration above, Eq. (14) should be considered in terms of the constitutive law for satisfying the internal force balance conditions of the entire system and matching the strain rate ($\dot{\gamma}_{\max}$) at each element based on the magnitude estimated from the local safety factor ($F_{s,local}$).

In addition, when a strain rate ($\dot{\gamma}_{\max}$) on the right side of Eq. (14) is exceeded in a certain time step, it is necessary to make a new action by incorporating an internal force (viscous resistance force), in which such forces retain the shear deformation of the elements, in order to keep it below the regulation value.

In a previous study, Sakuramoto et al. [60] proposed a model based on the nonlinear viscoelastic visco-plastic finite element method using an iterative method to model of the polymer materials for artificial joints, in which elastic-viscoelastic-viscoelastic elements are connected in series. The concept of the proposed models in this study is similar to that of Sakuramoto et al. [60] in the sense of viscoelasticity components as a visco-plasticity. However, the elements are not connected in the series of such three elements. Moreover, we have also prepared the iterative calculation algorithm for it.

Figure 8 shows a schematic diagram of the mechanical structure of the constitutive law, including the two types of viscous resistance. The strain increment ($\Delta\varepsilon$) based on the stress increment ($\Delta\sigma$) given to the element for each time step is divided into the elastic strain component ($\Delta\varepsilon^e$) and other components $\Delta\varepsilon^{vp}$, where $\Delta\varepsilon^{vp}$ occurs as the visco-plastic strain component ($\Delta\varepsilon^{vp}$) at first. However, the occurring magnitude of strain (strain rate) for each time step is regulated by Eq. (14); hence, there is no chance of further excessive shear strain for the elements in which $\dot{\gamma}_{\max}$ will exceed on the right side of Eq. (14). Thus,

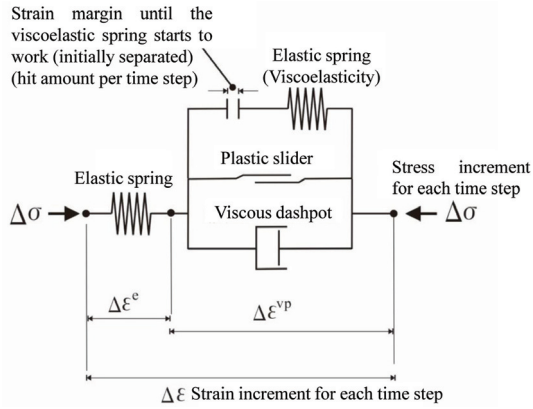

Fig. 8. Conceptual figure of the proposed constitutive model in this study.

the elastic response is restored, and the increase in strain is suppressed. This is the viscoelasticity, which is shown in the upper part of **Fig. 8**. Including this, the equivalent nodal force ($\boldsymbol{f}$) is calculated using Eq. (11), and the residual force ($\Delta\boldsymbol{r}$) is distributed throughout the entire system according to the modified Newton-Raphson method. Here, the stiffness of the viscoelastic spring is the same as the normal elastic spring, which contributes to the elastic stress increment before the yield limit.

Since the restoring force of this viscoelastic spring is temporarily generated as a resistance to sliding force for the time step, the restoring force is released for the next time step when the calculation of $\dot{\gamma}_{\max}$ is initialized. This means that when the occurring viscoelastic force is larger in the immediately previous time step, the load factor of the sliding force will also be greater in the next time step. Thus, even if the variation of $F_{s,local}$ greatly depends on the location on the slip surface, the shear stress is gradually redistributed from the concentration point to the adjacent element because the strain rate may exceed the upper limit of $\dot{\gamma}_{\max}$. Hence, the sliding velocity tends to be uniform.

Here, it should be noted that the cumulative amount of shear strain for each interested time step in Eq. (14) is the sum of the elastic component and visco-plastic component, and it does not include the strain caused by viscoelasticity after that. To reduce the occurrence of the exceeded strain on the right side of Eq. (14), the viscoelastic spring strain should be sufficiently smaller than the viscoelastic strain. Therefore, Young's modulus (E) of the material should not be too small. These points are the same as the discussions on how to give the rigidity when joint elements are used for modeling of the discontinuous surface characteristics [61].

3. Application of the Proposed Model

3.1. Landslide Field Experiment on a Natural Slope

The proposed model is applied to a landslide field experiment on a natural slope triggered by a rainfall

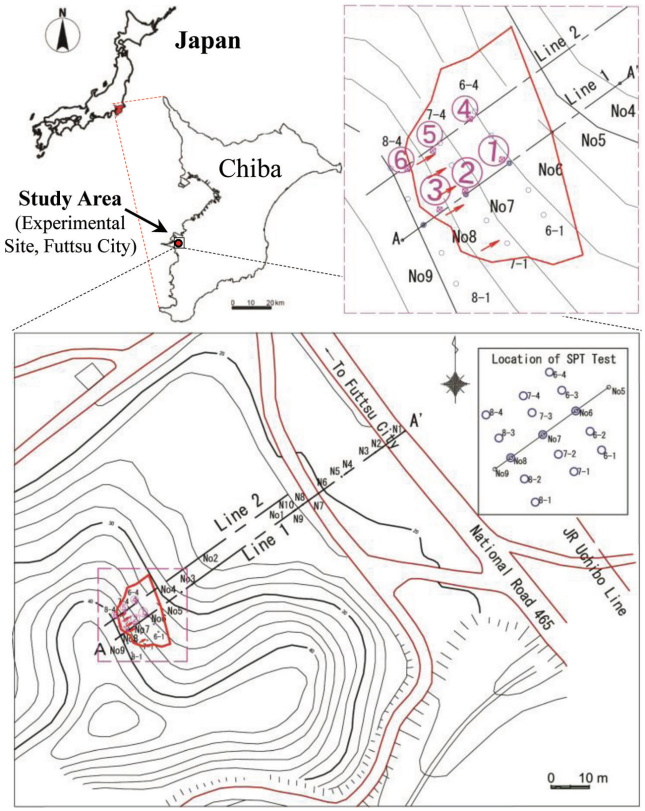

Fig. 9. Location of the study area and simplified topographical map of field test site in Futtsu City, Chiba Prefecture, Japan, showing the location of piezometers, water level gauges, extensometers, and tensiometers.

simulator in real time in Futtsu City, Chiba Prefecture, Japan (**Fig. 9**). **Fig. 9** shows the location of the study area and the simplified topographic map of the field test site, showing the location of the piezometers, water level gauges, extensometers, and tensiometers along line 1 of the X-section (A–A′) and line 2. The monitoring data along line 2 are not considered in this study. The size of the field experimental landslide measured approximately 20 m × 10 m, which spread by the precipitation intensity of 140–300 mm/h over an area of approximately 100 m^2 on the slope (**Fig. 10**). **Figs. 11–12** show the photographs of the experimental sites before and after the collapse.

The Standard Penetration Test (SPT) (Japanese Geotechnical Society, 2017) was performed at five locations of Nos. 6–8 to understand the tentative soil type of the test site and to locate the possible slip surface of the rainfall area (**Fig. 9**). At the location point of No. 6, a slip surface of 1.13 m from the ground level was observed. Similarly, a sliding surface depth of 0.84 m from the ground surface was recorded at No. 7, but there was not any sign of failure at No. 8. Based on the SPT test results and several videos captured during the experiment, the possible slip surface of the landslide was confirmed at approximately 1 m from the ground surface, as shown in **Fig. 10**.

The landslide field experiment using a rainfall simulator in real time was conducted on December 12, 2018.

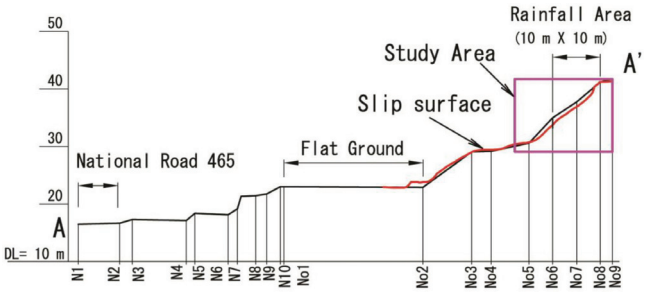

Fig. 10. Cross-sectional profile of the experimental slope along the line 1, A–A′.

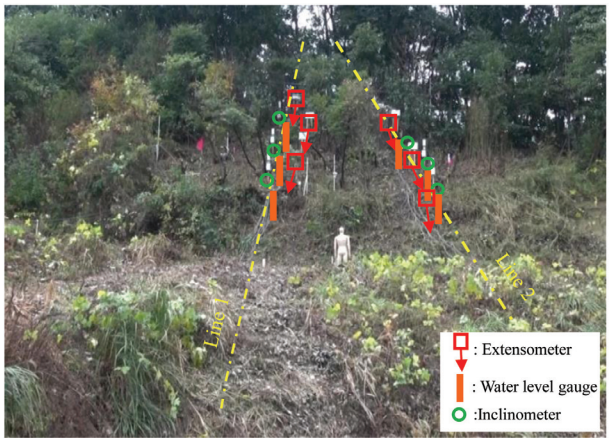

Fig. 11. Photograph of the field experimental site before collapse in Futtsu City, Chiba Prefecture, Japan, showing the location of piezometers, water level gauges, and extensometers.

Fig. 12. A representative photograph of the field experimental site after collapse.

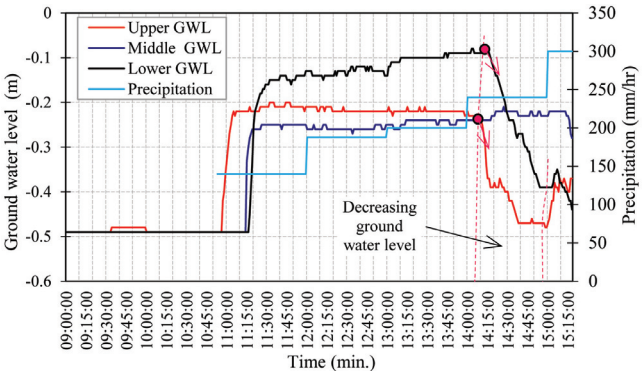

Fig. 13. Precipitation and groundwater fluctuation on the upper, middle, and lower water level gauges.

However, the pre-experiment was also conducted one day before by spreading a precipitation intensity of 140 mm/h for approximately one hour to adjust the distribution of precipitation on December 11, 2018. The real field experiment of the landslide was conducted at 10:53 a.m. on December 12, 2018, by spreading a maximum precipitation intensity of 140 mm/h approximately 10 m × 10 m (**Fig. 10**). The precipitation was increased to 188 mm/h at 12:00 p.m. Similarly, the precipitation was increased to 200 mm/h at 1:00 p.m. and 240 mm/h at 2:00 p.m. Finally, precipitation of 300 mm/h was fixed at 3:18 p.m., where the slope starts to apparently move after rainfall of 4 hours and 25 minutes (**Fig. 13**). The major objective of this study is to observe the creeping behaviors of a landslide induced by rainfall using finite element-based proposed methods, so the highlighted block in **Fig. 10** (i.e., 17 m × 12.63 m) was only considered for the FEM-based numerical simulation and analysis in this study. Six water level gauges and extensometers were installed at various locations of the slope along line 1 (close to A–A′) and line 2 for the measurement of the groundwater fluctuations and displacement rate with respect to time (**Fig. 9**). However, the recorded data along line 2 (i.e., ④, ⑤, and ⑥) are not considered in this study.

Figure 13 shows the precipitation and groundwater fluctuations on the upper slope (i.e., upper water level gauge or ③), middle slope (i.e., middle water level gauge or ②), and lower slope (i.e., lower water level gauge or ①). The groundwater level in the upper water level gauge began to rise at 10:57 a.m. after 3 minutes of precipitation of 140 mm/h, followed by the middle water level gauge and the lower water level gauge, respectively. The groundwater level in the upper water level gauge gradually increased by 0.27 m from 10:57 a.m. to 11:05 a.m. and remained almost constant until 2:09 p.m. Then, it suddenly decreased until 2:59 p.m. After spreading the precipitation of 300 mm/h, the groundwater level again rose (**Fig. 13**). In the case of the lower water level gauge, the groundwater level began to rise at 11:16 a.m. and gradually increased by 0.31 m until 11:26 a.m. Then, it also followed a similar pattern of fluctuations of groundwater in the upper water level gauge. However, the groundwater level began to rise at 11:15 a.m. in the middle water level gauge, and groundwater of 0.24 m gradually increased after about 10 minutes.

After this, the change in groundwater level was almost constant in all cases. Although the precipitation increased from 240 mm/h to 300 mm/h, the groundwater level suddenly decreased after 2:09 p.m. and 2:16 p.m. in the case of the upper water level gauge and lower water

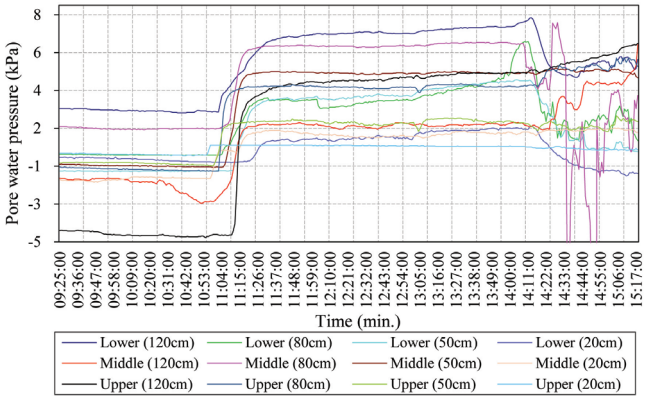

Fig. 14. Variations of the pore water pressures at the different depths on the upper, middle, and lower tensiometers.

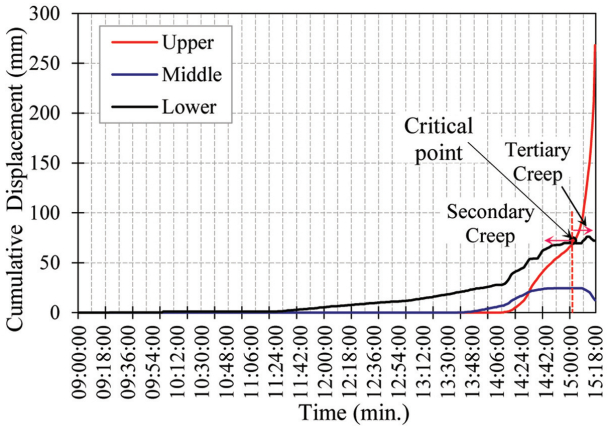

Fig. 15. Variations of the monitored cumulative displacement on the upper, middle, and lower extensometers.

level gauge, respectively. The reason behind the decreasing groundwater level was not clearly understood. However, the soil structure at different locations on the slope may change with changes in the slope. This change in soil structure may be due to the formation of soil blocks and changes in the distribution of large pores in the soil. During the movement of the landslide mass, there may be heterogeneous distribution of the groundwater in the soil surface, which may create a new discharge system with newly formed soil blocks. Moreover, the flow rate should also change with the change in slope. However, the change in flow rate was not measured during the experiments in this study.

Six tensiometers were buried at depths of 20 cm, 50 cm, 80 cm, and 120 cm along line 1 and line 2 for automatic measurement of the pore water pressure during the field experiment. **Fig. 14** shows the relation between the pore water pressure and time at the different depths on the lower, middle, and upper slope along line 1. After about 11:00 a.m., most of the tensiometers showed an increase in water pressure, and the fluctuations of the pore water pressure reading was almost constant until about 2:13 p.m., although the recorded value of the pore water pressure at the different depths were varying (**Fig. 14**). After that, most of the tensiometers recorded decreasing trends. However, the tensiometers at the depth of 120 cm in the middle followed the trend of increasing. After 2:00 p.m., 2:23 p.m., and 2:18 p.m., the increase/decrease in pore water pressure at a depth of 80 cm on the lower, middle, and upper slope were notable (**Fig. 14**). The reason behind the change in pore water pressure at the different depths should be related to the change in soil structures at the different depths.

Similarly, the corresponding extensometers recorded cumulative displacement with time, as presented in **Fig. 15**. From the analysis of the recorded displacement of the extensometer reading, it was understood that the slope began to move at 11:25 a.m. after gradually increasing the groundwater level (**Fig. 15**). The lower part (lower extensometer) of the landslide slope began to move first, followed by the middle extensometer and upper extensometer. The lower was slightly moving with an average constant displacement rate of 0.16 mm/min from 11:25 a.m. to 2:10 p.m. After that, the average constant displacement rate was slightly increased up to 2:47 p.m., and then, the displacement rate remained almost 0 after that. Similarly, an average constant displacement rate of 0.37 mm/min was recorded in the middle up to 2:40 p.m., but change in displacement remained almost 0 after that.

For recording and observing the overall phenomenon of the movement of the landslide mass, multiple cameras and video cameras were installed at different locations along the directions of line 1 and line 2 and fixed the time according to the Internet immediately before the beginning of the experiments to synchronize the time code on the videos. Based on the detailed observation and analysis of the recorded videos with time codes, it was found that the lower extensometer and middle extensometer were also moving along the same direction with the movement of the landslide mass. Therefore, those lower and middle extensometers along line 1 may not have measured the exact displacement of the landslide mass. In other words, the data recorded by the lower extensometer and middle extensometer may have some errors. Therefore, the lower extensometer and middle extensometer could not record the data of tertiary creep (**Fig. 15**). Hence, the change in displacement rate after 3:03 p.m. remains almost constant in the case of the lower extensometer and middle extensometer reading (**Fig. 15**).

In the case of the upper extensometer reading, a constant displacement rate of 0.1 mm/min was recorded in the beginning at 2:09 p.m., where the displacement rate of the lower extensometer was also increased. However, the average displacement rate gradually increased, and a displacement rate of 2.1 mm/min was reached at 3:03 p.m. After that, the displacement rate suddenly increased, leading to failure of the slope. Finally, the slope was totally collapsed after 3:18 p.m., with a displacement rate of 56.8 mm/min (i.e., last recorded data) (**Fig. 15**). Here,

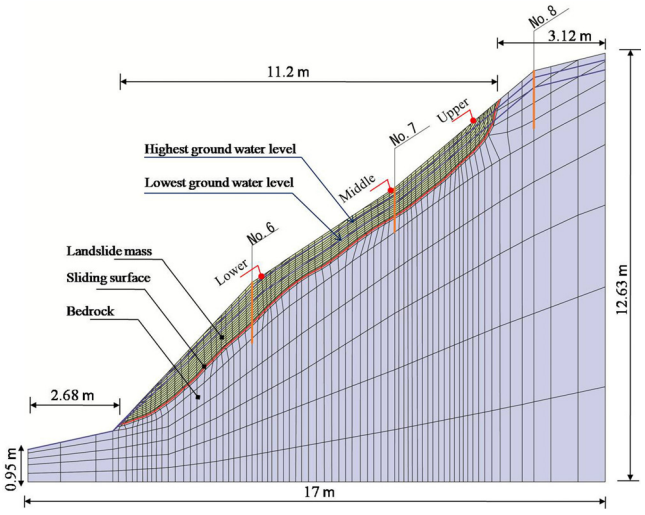

Fig. 16. Discretized finite element meshes with geological structure and groundwater level in the slope based on field investigations.

it seems that soil materials along the slip surface show the tertiary creep behaviors after 3:03 p.m. In the other word, the slip soil materials behave as the secondary stage of creep before 3:03 p.m. Therefore, the point (i.e., at time 3:03 p.m. along x-axis and equivalent cumulative displacement) is a critical point, from where the tertiary stage of creep began or, alternatively, the end point of the secondary stage of creep. As we have already discussed, the proposed models in this study are only capable of simulating the secondary creep behavior of soil materials along the sliding surface. Therefore, we have only considered up to the end point of the secondary stage of creep in this study. Therefore, the groundwater fluctuation data from 9:00 a.m. to 3:03 p.m. were only considered for numerical analysis in this study.

3.2. Numerical Modelling

The proposed numerical model is applied to an analysis of the creeping behavior of a landslide field experiment triggered by rainfall in real time of the natural slope in Futtsu City, Chiba Prefecture of Japan. **Fig. 16** shows the discretized finite element meshes with geological structure and groundwater level in the slope based on field investigations. The three major representative materials (layers) are assumed from the SPT test results of such landslide for simplification of the model. The weakest material (i.e., indicated by red in **Fig. 16**) was named "Sliding Surface." The thickness of this layer is assumed to be 1.0 cm. The soil materials are above the sliding surface, which were named "Sliding Mass" or "Landslide Mass." Similarly, it is assumed that the strongest material is below the sliding surface, which was referred as the "Bedrock." Here, the landslide mass and bed rock were modelled as solid elements and elastic bodies. However, the sliding surface was modelled with joint elements and assumed to be an elasto-viscoplastic body. The mesh adopted in the calculations consists of a rectangular element with eight nodes. The total number of 4800 nodes, 1531 elements, and 175 boundary conditions exist in the finite element model of the landslide body (**Fig. 16**). The base of the model (i.e., bottom boundary) was assumed to be fully impervious and fixed, and the lateral sides (right boundary and left boundary) were constrained by rollers. The hydraulic head of the maximum and minimum groundwater was imposed at the lateral boundaries based on the field monitoring results of groundwater fluctuation. In this study, the results of groundwater fluctuations from 9:00 a.m. to 3:03 p.m. were only considered (i.e., up to the secondary creep). The lower, middle, and upper were the nearest locations of points, where the displacement of the landslide body was measured during the field experiment (**Fig. 16**).

A parametric study was done to obtain the two new unknown control constitutive parameters $(\propto, n)$. Initially, the total factor of safety (F_s) of the landslide block is calculated using FEM. In FEM method, the shear strength reduction method (SSRM) is used to estimate the total factor of safety (F_s) of the field experimental landslide in Futtsu City. This method was originally proposed by Zienkiewicz et al. [59] for elasto-plastic finite element slope stability analysis. The details of the SSRM by FEM have been discussed by Zienkiewicz et al. [59], Ugai and Leshchinsky [62], Cai et al. [63], Cheng et al. [64], and Murakami et al. [65]. Using the abovementioned method, the total factor of safety owing to groundwater fluctuations caused by precipitation has been estimated for every minute. From the detailed analysis of the slope stability data using the FEM method, it was found that F_s were varied in a range of 0.98–1.020. After the calculation of F_s, the relations between $\dot{\gamma}_{\max}$ and F_s was established based on Eq. (14). After that, the general equations were obtained based on the well fitted curve between $\dot{\gamma}_{\max}$ and F_s. Then, the unknown two new control constitutive parameters $(\propto, n)$ were estimated by solving these general equations. On the other hand, the detailed field and laboratory studied were not performed on this landslide site. Therefore, effective strength parameters (c', φ') of the sliding surface were estimated based on the back analysis. The other requires simulation input parameters for each soil material (layers) are estimated based on different related reports and guidelines of textbooks. The estimated value of the unknown two new control constitutive parameters and the summary of the material parameters for landslide simulation are tabulated in **Table 1**.

3.3. Numerical Simulation Results and Discussion

Figure 17 shows the comparison of predicted time histories of displacement obtained from the numerical analysis and field monitoring data from the experiment. Here, the predicted time histories of displacement were measured at the same point in the upper, middle, and lower, where the landslide displacement was also measured during the field experiment. Moreover, the horizontal component of displacement was considered for predicting the time histories of displacement in the numerical model.

Table 1. Material parameters for each material.

Materials (→) / Parameters (↓)	Landslide Mass	Sliding Surface	Bed Rock
Young's modulus, E [kN/m^2]	10000	10000	100000
Poisson's ratio, ν	0.45	0.45	0.3
Cohesion force, c' [kN/m^2]	7	7	100
Internal friction angle, ϕ [°]	20	20	40
Dilatancy angle, ψ [°]	0	0	0
Unit weight, γ [kN/m^3]	18	18	22
$\dot{\alpha}$ [min^{-1}]	0.00031	0.00031	–
n	25	25	–

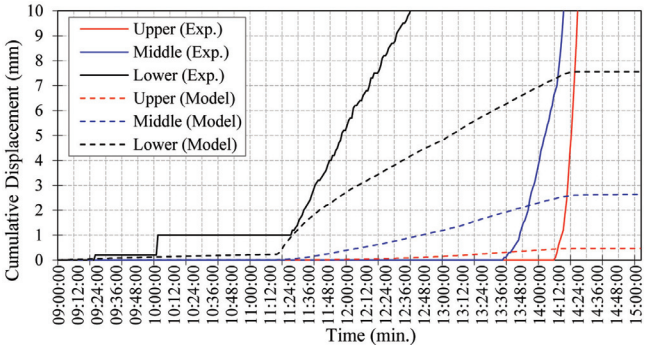

Fig. 17. Comparison of time histories of calculated sliding displacement of the sliding mass and observed extension on the upper, middle, and lower slope along line 1.

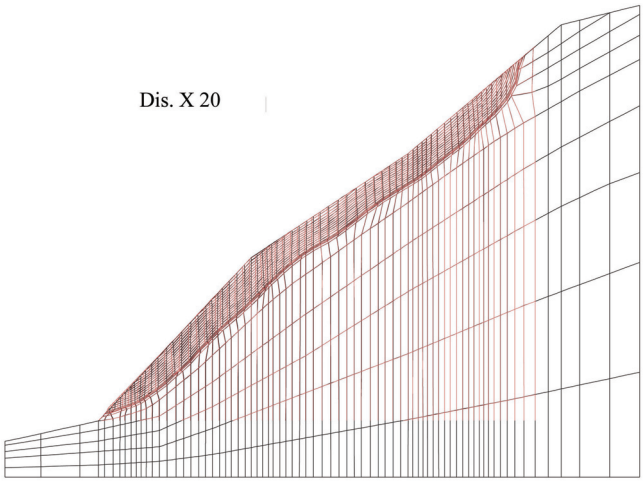

Fig. 18. Calculated residual deformation (exaggerated 20 times) after the final calculation step.

Figure 18 shows the results of the deformation pattern at the end (i.e., time = 3:03 p.m.) as a representative result. The red dotted line shows the result of a maximum deformation pattern of each node at the end of the numerical simulation with comparison to without the deformation (i.e., initial condition). Similarly, **Fig. 19** shows the results of the shear strain pattern at the end step of the calculation (i.e., time = 3:03 p.m.). From the comparative study of the field monitoring and numerical analysis results, it is found that the horizontal displacement at the same point of upper, middle, and lower was not perfectly matched to each other (**Fig. 17**).

In this study, the detail field and lab test to estimate the various soil parameters of each soil layer for the simulation were not performed. Therefore, the landslide simulation parameters of sliding mass, sliding surface, and bedrock were assumed based on the back calculation as well as trial methods. Moreover, material parameters of sliding mass and slip surface for numerical simulation were also assumed to be the same. The failure mechanisms along the slip surface due to the fluctuations of groundwater are not clearly known. From the videos that were taken by the NHK from the multiple cameras installed in different locations, we observed that the slip surface contained much water immediately after the occurrence of the landslides. It also pulled out and brooked the roots along the slip surface after the landslide (**Fig. 12**). Therefore, the failure mechanisms along the slip surface of the natural slope should be known to obtain better simulation results. However, we briefly discuss the possible failure mechanisms along the slip surface of such a slope based on the simulation analysis results in the paragraphs below. On the other hand, the groundwater level decreased in the upper and middle after 2:09 p.m. and 2:16 p.m., respectively, whereas the movement rate after that time was almost constant (i.e., secondary stage of creep) until 3:03 p.m. The interesting point is the major causes of suddenly decreasing groundwater level despite the constant movement (i.e., secondary creep behaviors) of the landslide mass. Therefore, the measured and predicted time histories were not good agreements with each other (**Fig. 17**). Thus, the numerical simulation up to the tertiary stage of creep has been demanded to obtain better simulation results of such type of landslides. Hence, we believe that such proposed models will be extended or modified to simulate the tertiary creep behaviors of slope or landslide triggered by rainfall in the near future. It is

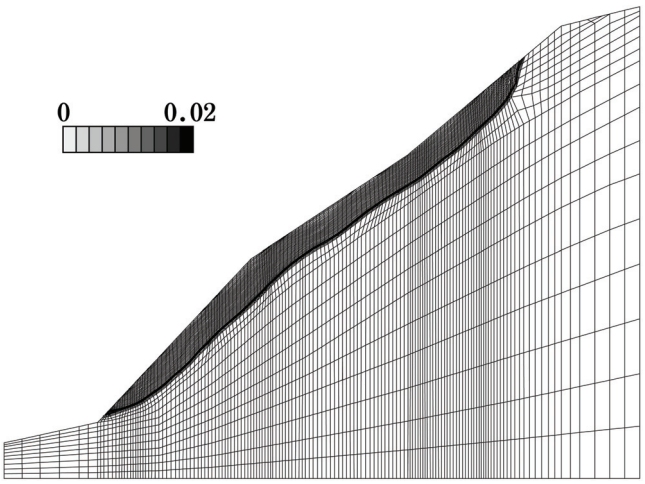

Fig. 19. Calculated maximum shear strain distributions after the final calculation step.

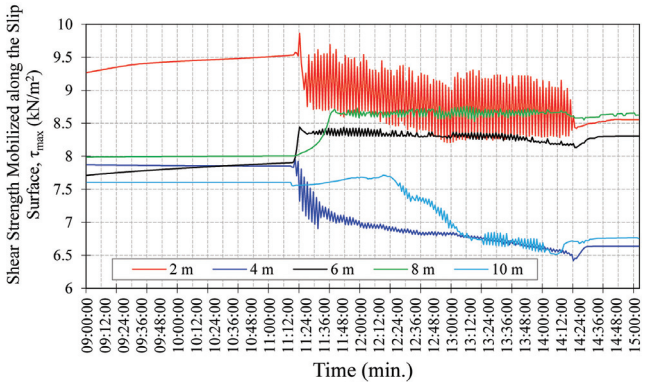

Fig. 20. Change of calculated shear strength mobilized along slip surface in time.

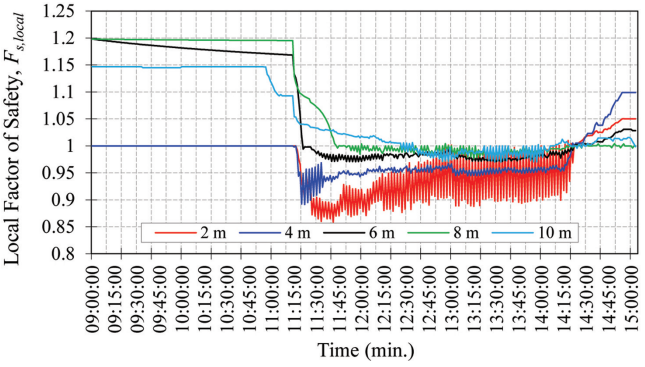

Fig. 21. Calculated time histories of the local factor of safety at each element along slip surface.

expected that such extended study will be useful for predicting the creep displacement behaviors of slope failure or landslides triggered by rainfall, and at the same time, countermeasure works for long-term prevention and mitigation from such type of landslide in monsoon Asia will be easier in the near future.

Skempton [66, 67] has suggested that the drained residual strength is mobilized along pre-existing shear surfaces of a creeping landslide. Picarelli et al. [31] have suggested that continuous translative movements of slopes may be the result of cyclic pore pressure changes along the slip surface, causing shear strength to be mobilized along the slide/slip surface. Vulliet and Hutter [54] have also agreed with Picarelli et al. [31]. The main cause of landslide displacement is due to the increase of the mobilized shear stress, in which weight of surcharge above the potential failure may be increased because of rising of groundwater levels. This means that when the groundwater level is raised, the pore water pressure is also increased along the slip surface. Hence, the effective stress will be decreased, and the mobilized shear stress will be greater than the effective stress. Then, the soil mass begins to move slowly at first, finally leading to failure. In other words, the normal stress is decreasing with the increase in groundwater level, and the driving force becomes equal to or slightly greater than the resisting force, which leads to failure or moving of the landslide body. Picarelli et al. [31] have reported that increasing pore water pressure decreases the shear strength of the soil, which may lead to slope failure.

To check the details of the failure mechanisms, the shear resistance mobilized and variation of local factor of safety along the sliding surface have been also studied. **Fig. 20** shows the change of calculated shear strength mobilized along the slip surface in time. Similarly, the calculated time histories of the local factor of safety at each element along the slip surface are shown in **Fig. 21**. The distance of the interested points was selected in an equal horizontal distance (i.e., 2-m interval) from the toe of slope (i.e., the coordinate of the toe was assumed zero). The shear resistance mobilized along the slip surface was slightly increased from the beginning (at 10:53 a.m.) to 11:15 a.m. for all the observed distances, but after that, it was suddenly increasing (**Fig. 20**). On the other hand, the change in the local factor of safety for all observed distances along the slip surface was found almost constant up to 11:20 a.m. After that, the local factor of safety along the slip surface was suddenly decreased, which may lead to movement of the landslide mass (**Fig. 21**). Based on the comparative study of the numerical analysis results of the local factor of safety and shear strength mobilized along the slip surface in time, it was understood that the mobilized shear strength along the slip surface near to toe (i.e., 2 m) was high, whereas the local factor of safety at the same location was also low, and vice versa (**Figs. 20–21**). From an analysis of the field monitoring results, the movement of the slope was beginning near the toe (i.e., lower) at first at 11:25 a.m. Therefore, such numerical analysis results were also good agreements with the field monitoring results of displacement in the case of initiating the movement of the slope. Thus, it can be concluded that the shear strength mobilized along the slip surface has a major role in triggering the landslide. Hence,

the failure mechanism of a creeping landslide is strongly dependent on shear stress mobilized along the slip surface due to the change in groundwater level. Previous researchers (e.g., [2, 30, 31, 34]) have also agreed on this.

4. Concluding Remarks

This paper has primarily addressed the stress-dependent landslide movements with groundwater fluctuations with the help of newly developed FEM-based numerical models and numerical analysis results and has provided an insight for disaster prevention in monsoon Asia. A two-dimensional elasto-viscoplastic constitutive model has been used to simulate the secondary creeping behavior of the sliding surface soil materials of rainfall-induced landslides. The major findings of this study include the following:

(1) As an example, the current scenario of creeping landslides in Nepal and Japan have been briefly discussed, and possible landslide sites for further application of the proposed numerical models in the near future have also been presented.
(2) The novel numerical approaches have been proposed to understand the secondary creep behavior of the landslide owing to groundwater fluctuations by rainfall.
(3) A simplified procedure for the determination of new control constitutive parameters has been developed. Two control constitutive parameters have been incorporated for the first time to assess the realistic field problem of landslides triggered by rainfall.
(4) Such constitutive parameters can easily be estimated based on the relation between the total factor of safety (F_s) and the sliding velocity ($\dot{\gamma}_{max}$).
(5) In previous studies, understanding the creeping behavior of landslides seemed almost impossible without detailed field monitoring data and detailed field and laboratory investigations. However, the proposed models are useful for better understanding the creep displacement behaviors of landslides by directly changing the control constitutive parameters and other simulation parameters for each soil material. Moreover, this study may be useful for predicting the displacement rate of landslides caused by extreme rainfall.
(6) The proposed models have been applied to a landslide field experiment on a natural slope in the Futtsu City of Chiba Prefecture, Japan, to check the applicability of the novel models in real field problems of slope failure and landslide.
(7) The measured (experimental) and predicted (model) time histories along the horizontal direction have been compared, and slightly different results were found with each. The possible causes of such differences have also been discussed.
(8) Based on the numerical analysis results of the field experiment landslide, the details of the deformation pattern, shear strain pattern, and possible causes of slope failure mechanisms have been discussed.

The proposed numerical methods have been applied to study the creep displacement behavior of few landslides case studies until now. However, it will be continuously applied to many other rainfall-induced landslides, with variation of groundwater level to check for further applicability of such proposed models. Moreover, such models are only prepared for the numerical simulation of secondary stage of creep. Therefore, further modification or extension of such models is necessary for the numerical analysis of tertiary creep behavior of landslides in the near future.

Acknowledgements

The authors would like to acknowledge Mr. Yosuke Koyama (NHK: Japan Broadcasting Corporation) for the overall planning and preparation of the field experiments. The authors would like to thank the Japan Forest Technics Co. for conducting the preliminary survey of the experimental site. The authors wish to thank the OSASI Technos Inc. and Daiki Rika Kogyo Co., Ltd. for providing the necessary measuring equipment for the experiment and their cooperation during the field measurements. The authors are also grateful to Futtsu City, a Federation of Five Construction Firms in Futtsu City, the Chiba Prefectural Police, and the Department of Civil Engineering, Chiba Prefecture, for their support and cooperation during the field experiments. The authors would also like to thank the editor and two reviewers for their critical and helpful reviews to improve the quality of this paper. This work has also been supported by JSPS-KAKENHI Grant Number 18H01674.

References:

[1] K. Terzaghi, "Mechanism of Landslide," S. Paige (Ed.), "Application of Geology to Engineering Practice: Berkey Volume," pp. 83-123, Geological Society of America, 1950.
[2] G. Ter-Stepanian, "On the Long Term Stability of Slopes," Norwegian Geotechnical Institute (NGI) Publication No.52, pp. 1-14, 1963.
[3] H. Eyring, "Viscosity, Plasticity, and Diffusion as Example of Absolute Reaction Rates," J. Chem. Phys., Vol.4, pp. 283-291, 1936.
[4] E. Shimokawa, "Creep Deformation of Cohesive Soils and its Relationship to Landslide," Mem. Fac. Agr. Kagoshima. Univ., Vol.16, pp. 129-156, 1980.
[5] J. Feda, "Interpretation of Creep of Soil by Rate Process Theory," Géotechnique, Vol.39, No.4, pp. 667-677, 1989.
[6] S. Murayama and T. Shibata, "Rheological Properties of Clay," Proc. of the 5th Int. Conf. on Soil Mechanics and Foundation Engineering, Part 1, pp. 269-273, 1961.
[7] R. W. Christensen and T. H. Wu, "Analysis of Clay Deformation as Rate Process," J. Soil Mech. Found. Div., Vol.90, No.6, pp. 125-157, 1964.
[8] G. Ter-Stepanian, "Creep of a Clay During Shear and its Rheological Model," Géotechnique, Vol.25, No.2, pp. 299-320, 1975.
[9] B. C. Yen, "Stability of Slopes Undergoing Creep Deformation," J. Soil. Mech. Found. Div., Vol.95, No.4, pp. 1075-1096, 1969.
[10] J. N. Suhaydu and D. B. Prior, "Explanation of Submarine Landslide Morphology by Stability Analysis and Rheological Models," Proc. of 10th Offshore Technol. Conf., pp. 1075-1082, 1978.
[11] R. M. Iverson, "A Constitutive Equation for Mass-Movement Behavior," J. Geol., Vol.9, No.3, pp. 143-160, 1985.
[12] H. Sekiguchi and H. Ohta, "Induced Anisotropy and Time Dependency in Clays," Proc. of the 9th Int. Conf. on Soil Mechanics and Foundation Engineering (ICSMFE), pp. 229-238, 1977.
[13] C. Zhou, J.-H. Yin, J.-G. Zhu, and C.-M. Cheng, "Elastic Anisotropic Viscoplastic Modeling of the Strain-Rate-Dependent Stress-Strain Behaviour of K_0-Consolidated Natural Marine Clays in Triaxial Shear Test," Int. J. Geomech., Vol.5, No.3, pp. 218-232, 2006.

[14] C. S. Desai, N. C. Samtani, and L. Vulliet, "Constitutive Modeling and Analysis of Creeping Slopes," J. Geotech. Eng., Vol.121, No.1, pp. 43-56, 1995.

[15] J. M. Pestana and A. J. Whittle, "Formulation of a Unified Constitutive Model for Clays and Sands," Int. J. Numer. Anal. Meth. Geomech., Vol.23, No.12, pp. 1215-1243, 1999.

[16] S. J. Wheeler, A. Näätänen, M. Karstunen, and M. Lojander, "An Anisotropic Elastoplastic Model for Soft Clays," Can. Geotech. J., Vol.40, No.2, pp. 403-418, 2003.

[17] Y. F. Dafalias, M. T. Manzari, and A. G. Papadimitriou, "SANICLAY: Simple Anisotropic Clay Plasticity Model," Int. J. Numer. Anal. Meth. Geomech., Vol.30, No.12, pp. 1231-1257, 2006.

[18] M. Leoni, M. Karstunen, and P. A. Vermeer, "Anisotropic Creep Model for Soft Soils," Géotechnique, Vol.58, No.3, pp. 215-226, 2008.

[19] M. Liingaard, A. Augustesen, and P. V. Lade, "Characterization of Models for Time-Dependent Behavior of Soils," Int. J. Geomech., Vol.4, No.3, pp. 157-177, 2004.

[20] M. Calvello, L. Cascini, and G. Sorbino, "A Numerical Procedure for Predicting Rainfall-Induced Movements of Active Landslides Along Pre-Existing Slip Surfaces," Int. J. Numer. Anal. Meth. Geomech., Vol.32, No.4, pp. 327-351, 2008.

[21] N. Huvaj and A. Maghsoudloo, "Finite Element Modeling of Displacement Behavior of a Slow-Moving Landslide," Proc. of Geo-Congress 2013, pp. 670-679, 2013.

[22] J. A. Fernández-Merodo, J. C. García-Davalillo, G. Herrera, P. Mira, and M. Pastor, "2D Viscoplastic Finite Element Modelling of Slow Landslides: The Portalet Case Study (Spain)," Landslides, Vol.11, No.1, pp. 29-42, 2014.

[23] D. R. Bhat, N. P. Bhandary, R. Yatabe, and R. C. Tiwari, "Residual-State Creep Test in Modified Torsional Ring Shear Machine: Methods and Implications," Int. J. of GEOMATE, Vol.1, No.1, pp. 39-43, 2011.

[24] D. R. Bhat, N. P. Bhandary, R. Yatabe, and R. C. Tiwari, "A New Concept of Residual-State Creep Test to Understand the Creeping Behavior of Clayey Soils," Proc. of GeoCongress 2012, pp. 683-692, 2012.

[25] D. R. Bhat, N. P. Bhandary, and R. Yatabe, "Residual-State Creep Behavior of Typical Clayey Soils," Nat. Hazards, Vol.69, No.3, pp. 2161-2178, 2013.

[26] D. R. Bhat, R. Yatabe, and N. P. Bhandary, "Creeping Displacement Behavior of Clayey Soil in a New Creep Test Apparatus," Proc. of Geo-Shanghai 2014, pp. 275-285, 2014.

[27] D. R. Bhat and R. Yatabe, "A Regression Model for Residual State Creep Failure," Proc. of 18th Int. Conf. on Soil Mechanics and Geotechnical Engineering, pp. 707-711, 2016.

[28] E. Conte, A. Donato, and A. Troncone, "A Finite Element Approach for the Analysis of Active Slow-Moving Landslides," Landslides, Vol.11, No.4, pp. 723-731, 2014.

[29] Y. Ishii, K. Ota, S. Kuraoka, and R. Tsunaki, "Evaluation of Slope Stability by Finite Element Method Using Observed Displacement of Landslide," Landslides, Vol.9, No.3, pp. 335-348, 2012.

[30] E. Eberhardt, L. Bonzanigo, and S. Loew, "Long-Term Investigation of a Deep-Seated Creeping Landslide in Crystalline Rock. Part II. Mitigation Measures and Numerical Modelling of Deep Drainage at Campo Vallemaggia," Can. Geotech. J., Vol.44, No.10, pp. 1181-1199, 2007.

[31] L. Picarelli, G. Urciuoli, and C. Russo, "Effect of Groundwater Regime on the Behaviour of Clayey Slopes," Can. Geotech. J., Vol.41, No.3, pp. 467-484, 2004.

[32] H. G. Brandes and D. D. Nakayama, "Creep, Strength and Other Characteristics of Hawaiian Volcanic Soils," Géotechnique, Vol.60, No.4, pp. 235-245, 2010.

[33] J. D. Nelson and E. G. Thompson, "A Theory of Creep Failure in Overconsolidated Clay," J. Geotech. Eng. Div., Vol.103, No.11, pp. 1281-1294, 1977.

[34] F. D. Patton, "Groundwater Pressure and Stability Analyses of Landslides," Proc. of the 4th Int. Symp. on Landslides, Vol.3, pp. 43-60, 1984.

[35] L. K. Walker, "Undrained Creep in a Sensitive Clay," Géotechnique, Vol.19, No.4, pp. 515-529, 1969.

[36] Z.-Y. Yin, C. S. Chang, M. Karstunen, and P.-Y. Hicher, "An Anisotropic Elastic–Viscoplastic Model for Soft Clays," Int. J. Solids and Struct., Vol.47, No.5, pp. 665-677, 2010.

[37] W. Z. Savage and A. F. Chleborad, "A Model for Creeping Flow in Landslides," Bull. Assoc. Eng. Geol., Vol.19, No.4, pp. 333-338, 1982.

[38] K. Forbes and J. Broadhead, "Forests and Landslides: The Role of Trees and Forests in the Prevention of Landslides and Rehabilitation of Landslide-Affected Areas in Asia," p. 3, Rap Publication, 2011.

[39] R. K. Dahal, "Rainfall-Induced Landslides in Nepal," Int. J. Eros. Control Eng., Vol.5, No.1, pp. 1-8, 2012.

[40] S. Hasegawa, R. K. Dahal, M. Yamanaka, N. P. Bhandary, R. Yatabe, and H. Inagaki, "Causes of Large-Scale Landslides in the Lesser Himalaya of Central Nepal," Environ. Geol., Vol.57, No.6, pp. 1423-1434, 2009.

[41] D. N. Petley, G. J. Hearn, A. Hart, N. J. Rosser, S. A. Dunning, K. Oven, and W. A. Mitchell, "Trends in Landslide Occurrence in Nepal," Nat. Hazards, Vol.43, pp. 23-44, 2007.

[42] D. R. Bhat and A. Wakai, "Investigation of Creeping Landslides Along the Major Highway of Nepal Triggered by the 2015 Gorkha, Nepal Earthquake," Proc. of the Research Committee on Strong Linear Phenomena of Surface Ground and its Effects at the Great Earthquake Symp., Ground Society Association of GeoKanto, pp. 77-80, 2018.

[43] Japan Landslide Society and National Conference of Landslide Control, "Landslides in Japan," 6th Revision, 2002.

[44] A. Wakai, D. R. Bhat, K. Kotani, and S. Osawa, "Numerical Simulation of a Creeping Landslide Case in Japan," B. Tiwari, K. Sassa, P. T. Bobrowsky, K. Takara (Eds.), "Understanding and Reducing Landslide Disaster Risk: Volume 4 – Testing, Modeling and Risk Assessment," pp. 273-280, Springer, 2021.

[45] D. R. Bhat, R. Yatabe, and N. P. Bhandary "Study of Preexisting Shear Surfaces of Reactivated Landslides from a Strength Recovery Perspective," J. Asian Earth Sci., Vol.77, pp. 243-253, 2013.

[46] D. R. Bhat, A. Wakai, and K. Kotani, "A Finite Element Approach to Understand the Creeping Behaviour of Large-Scale Landslides," Proc. of the 19th Int. Summer Symp., pp. 9-10, 2017.

[47] D. R. Bhat and A. Wakai, "Numerical Simulation of a Creeping Landslide Induced by a Snow Melt Water," Technical J., Vol.1, No.1, pp. 71-78, 2019.

[48] H. Saito, O. Korup, T. Uchida, S. Hayashi, and T. Oguchi, "Rainfall Conditions, Typhoon Frequency, and Contemporary Landslide Erosion in Japan," Geology, Vol.42, No.11, pp. 999-1002, 2014.

[49] Y. Hong, H. Hiura, K. Shino, K. Sassa, A. Suemine, H. Fukuoka, and G. Wang, "The Influence of Intense Rainfall on the Activity of Large-Scale Crystalline Schist Landslides in Shikoku Island, Japan," Landslides, Vol.2, No.2, pp. 97-105, 2005.

[50] Y. Sasaki, A. Fujii, and K. Asai, "Soil Creep Process and its Role in Debris Slide Generation – Field Measurements on the North Side of Tsukuba Mountain in Japan," Eng. Geol., Vol.56, Nos.1-2, pp. 163-183, 2000.

[51] S. Ogita, W. Sagara, D. Higaki, and Research Committee on Elucidating Mechanisms of Large-Scale Landslides, "Shapes and Mechanisms of Large-Scale Landslides in Japan: Forecasting Analysis from an Inventory (WCoE 2014–2017)," K. Sassa, M. Mikoš, and Y. Yin (Eds.), "Advancing Culture of Living with Landslides: Vol.1 – ISDR-ICL Sendai Partnerships 2015–2025," pp. 315-324, Springer, 2017.

[52] H. Yagi and T. Inokuchi, "Aerial Watching of Landslides in Japan -26- Jin-Nosuke-Dani Landslide, Mt. Hakusan, Central Japan," J. Jpn. Landslide Soc., Vol.49, No.6, pp. 348-349, 2012.

[53] H. Yagi and T. Inokuchi, "Aerial Watching of Landslides in Japan -50- Epilogue of the Series "Aerial Watching of Landslides in Japan,"" J. Jpn. Landslide Soc., Vol.54, No.6, pp. 289-293, 2017.

[54] L. Vulliet and K. Hutter, "Viscous-Type Sliding Laws for Landslides," Can. Geotech. J., Vol.25, No.3, pp. 467-477, 1988.

[55] N. Sugawara, "Variation of Surface Displacement Rate with Factor of Safety for Creep-Type Landslides (As a Consequence from Reviewing Literatures)," Oyo Technical Report, No.23, pp. 1-18, 2003 (in Japanese with English Abstract).

[56] D. R. Bhat, A. Wakai, and K. Kotani, "A Comparative Study of Two Newly Developed Numerical Models to Understand the Creeping Behaviour of Landslides," Proc. of the 20th Int. Summer Symp., pp. 101-102, 2018.

[57] The Japanese Geotechnical Society, "FEM Series 3 for Ground Engineers: Using the Elasto-Plastic Finite Element Method," 2003 (in Japanese).

[58] T. Tanaka, "Deformation and Stability Analysis by Finite Element Method," The Japanese Society of Soil Mechanics and Foundation Engineering, "Principle of Soil Mechanics," 1st Revision, pp. 109-154, 1992 (in Japanese).

[59] O. C. Zienkiewicz, C. Humpheson, and R. W. Lewis, "Associated and Non-Associated Visco-Plasticity and Plasticity in Soil Mechanics," Géotechnique, Vol.25, No.4, pp. 671-689, 1975.

[60] I. Sakuramoto, T. Tsuchida, K. Kuramoto, and S. Kawano, "A Study on Nonlinear Viscoelastic Viscoplastic Finite Element Method Using Iterative Method," Trans. Jpn. Soc. Mech. Eng. A, Vol.66, No.651, pp. 1984-1989, 2000 (in Japanese with English Abstract).

[61] The Japanese Geotechnical Society, "Japanese Geotechnical Society Q & A," Vol.2, pp. 276-278, 2009 (in Japanese).

[62] K. Ugai and D. Leshchinsky, "Three-Dimensional Limit Equilibrium and Finite Element Analysis: A Comparison of Results," Soils Found., Vol.35, No.4, pp. 1-7, 1995.
[63] F. Cai, K. Ugai, A. Wakai, and Q. Li, "Effects of Horizontal Drains on Slope Stability Under Rainfall by Three-Dimensional Finite Element Analysis," Comput. Geotech., Vol.23, No.4, pp. 255-275, 1998.
[64] Y. M. Cheng, T. Lansivaara, and W. B. Wei, "Two-Dimensional Slope Stability Analysis by Limit Equilibrium and Strength Reduction Methods," Comput. Geotech., Vol.34, No.3, pp. 137-150, 2007.
[65] A. Murakami, A. Wakai, and K. Fujisawa, "Numerical Methods," Soils Found., Vol.50, No.6, pp. 877-892, 2010.
[66] A. W. Skempton, "Long-Term Stability of Clay Slopes," Géotechnique, Vol.14, No.2, pp. 77-102, 1964.
[67] A. W. Skempton, "Residual Strength of Clays in Landslides, Folded Strata and the Laboratory," Géotechnique, Vol.35, No.1, pp. 3-18, 1985.

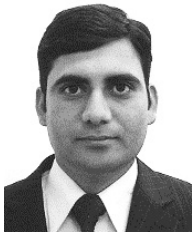

Name:
Deepak Raj Bhat

Affiliation:
Chief (Research) Engineer, Okuyama Boring Co., Ltd.

Address:
5F Goto Building, 3-5-9 Higashi-Nihonbashi, Chuo-ku, Tokyo 103-0004, Japan

Selected Publications:
• "Residual-state creep behavior of typical clayey soils," Nat. Hazards, Vol.69, No.3, pp. 2161-2178, 2013.
• "Study of preexisting shear surfaces of reactivated landslides from a strength recovery perspective," J. Asian Earth Sci., Vol.77, pp. 243-253, 2013.

Name:
Soichiro Osawa

Affiliation:
Graduate Student, Geotechnical Engineering Laboratory, Department of Environmental Engineering Science, Gunma University
Address:
1-5-1 Tenjincho, Kiryu, Gunma 376-8515, Japan

Name:
Akihiko Wakai

Affiliation:
Professor, Gunma University
Address:
1-5-1 Tenjincho, Kiryu, Gunma 376-8515, Japan

Name:
Katsuo Sasahara

Affiliation:
Professor, Science and Technology Unit, Natural Sciences Cluster, Research and Education Faculty, Kochi University
Address:
2-5-1 Akebonocho, Kochi, Kochi 780-8520, Japan

Name:
Netra P. Bhandary

Affiliation:
Professor, Faculty of Collaborative Regional Innovation, Ehime University
Address:
3 Bunkyo-cho, Matsuyama, Ehime 790-8577, Japan

Name:
Fei Cai

Affiliation:
Associate Professor, Gunma University
Address:
1-5-1 Tenjincho, Kiryu, Gunma 376-8515, Japan

Name:
Hirotaka Ochiai

Affiliation:
Technical Adviser, Japan Forest Technology Association (JAFTA)
Address:
7 Rokubancho, Chiyoda-ku, Tokyo 102-0085, Japan

Name:
Norihiro Tanaka

Affiliation:
Tokyo Office Chief, Chief (Research) Engineer, Okuyama Boring Co., Ltd.
Address:
5F Goto Building, 3-5-9 Higashi-Nihonbashi, Chuo-ku, Tokyo 103-0004, Japan